Simultaneous reconstruction of dielectric and perfectly conducting scatterers via *T*-matrix method

Xiuzhu Ye, Xudong Chen, Yu Zhong and Rencheng Song

***Abstract*— A *T*-matrix method is proposed to solve the mixed boundary inverse scattering problem, i.e., perfect electric conductors (PEC) and dielectric scatterers are simultaneously reconstructed under the two-dimensional transverse magnetic (TM) illumination setting. Both the dipole and monopole elements of the *T*-matrix are chosen to accurately describe the scattering behavior of the mixed boundary problem. Criteria of utilizing the monopole element of *T*-matrix to distinguish the PEC from dielectric scatterers are presented. Apart from synthetic data, the experimental data from Fresnel dataset is also used to verify the validity of the proposed method, showing that it works well in sub-wavelength setting and is quite robust against noise. The pros and cons of the proposed *T*-matrix method are further discussed.**

***Index Terms*— Inverse scattering, *T*-matrix, Optimization**

I. Introduction

The inverse scattering problem has been studied for decades and a lot of methodologies have already been well developed for dielectric scatterer [1-7] and perfect electric conductor (PEC) [8-12] respectively. The modeling schemes are mostly based on the electric field integral equation (EFIE) [13]. Mixed boundary inverse scattering problem refers to the problem where PEC and dielectric scatterers are simultaneously present inside the detection domain. Qualitative methods such as linear sampling method[14], multiple signal classification (MUSIC) algorithm and factorization method[15] are able to solve the mixed boundary inverse problem, which retrieve the shape and number of scatterers only. In quantitative reconstruction, the properties of the scatterers are extra unknowns to be solved and the target is to identify the shape of the PEC scatterers while at the same time to reconstruct the spatial distribution of the relative permittivity for dielectric scatterer. To quantitatively reconstruct the mixed boundary problem under EFIE model, one existing solution is to approximate the PEC scatterers by lossy dielectric scatterers and thus both dielectric and PEC scatterers can be represented by complex relative permittivity [16-19]. The PEC is distinguished from the dielectric scatterers by the higher imaginary part. However, due to the approximation taken, the method may fail in the case when both high-loss dielectric scatterers and PEC are present.

In this paper, we provide another quantitative method under a new modeling scheme--the *T*-matrix method, to solve the mixed boundary inverse problem. The *T*-matrix method was firstly developed by Waterman in 1965 [20] and further adopted by Chew [21-23] to solve the inverse scattering problem. In *T*-matrix method, the scattered and incident fields are firstly expanded as functions of multipoles, and then scattered field coefficient is related to the incident field coefficient by *T*-matrix only utilizing the boundary condition. Different properties of scatterers have different finite valued *T*-matrices. Thus, the *T*-matrix method provides a possibility of modeling the mixed boundary problem. In this paper, subspace based optimization method (SOM) is further extended to the *T*-matrix modeling method to solve the mixed boundary problem, which has already been extensively used for either PEC [11, 12] or dielectric scatterers [3-5, 24] under the EFIE modeling scheme owing to its robustness against noise and fast convergence speed.

The differences of the proposed method compared to the original *T*-matrix inversion methods are listed as follows. Firstly, in the original *T*-matrix based inverse scattering method, scatterers are known to be perfectly conducting [21] or dielectric [22, 23] *a priori*. Thus, only single leading multipole term is sufficient in modeling the scattering behavior of the PEC or dielectric scatterers respectively. To be specific, only the monopole term is used to model the scattering of PEC scatterers for 2D TM incidence [21], whereas only the dipole term is used to model the scattering of dielectric scatterers for 2D TE incidence [22] and 3D case [23]. In our paper, we consider a mixture of two kinds of scatterers for 2D TM incidence. Although the monopole term is leading for both PEC and dielectric scatterers individually, it is inaccurate to use only one multipole to model the scattering behavior for mixed boundary problem, due to the fact that dipole term of PEC scatterer is comparable in magnitude to the monopole term of dielectric scatterer. Thus both the monopole and dipole terms are chosen to describe the scattering behavior for mixed boundary problem, to ensure the accuracy of calculated scattered field. Secondly, in the original *T*-matrix inversion methods [21-23], the properties of scatterers are known *a*

Manuscript received May 11th, 2012. This work was supported by the Singapore Temasek Defence Systems Institute under grant TDSI/10-005/1A.

The authors are with department of Electrical and Computer Engineering, National University of Singapore, 117576 Singapore, Singapore(e-mail: g0800455@nus.edu.sg, elechenx@nus.edu.sg, elezhong@nus.edu.sg, elesongr@nus.edu.sg)

priori. In our paper, no *a priori* information is needed in identifying the properties of scatterers. The monopole element in *T*-matrix of each subunit is used to classify the PEC scatterers from the dielectric ones.

The main contributions of the proposed *T*-matrix method are: Firstly, the *T*-matrix method has provided an alternative modeling method to quantitatively deal with mixed boundary problem, which is different from the contemporary EFIE modeling methods [16-19] that treat PEC scatterer as high-loss dielectric scatterer. Secondly, the *T*-matrix method has provided a new criterion in differentiating the PEC from dielectric scatterers. It works well no matter the dielectric scatterers are lossy or not, which is an advantage over the contemporary method [16-19]. Thirdly, SOM has been applied in the framework of *T*-matrix modeling method, showing that the SOM is a general method which is not limited to EFIE modeling. Lastly, the success of reconstructions from various synthetic data as well as experimental data shows the validity of the proposed *T*-matrix based inversion method.

II. Forward Problem

A. Experimental Setup

In this paper, we consider the inverse scattering problem in a two-dimensional setting under the transverse magnetic (TM) time harmonic illuminations. The setup of this problem is depicted as in Fig.1. For the convenience of reading, in this paper, we use italic characters to denote scalars (such as c). We use bold body or character with head bar to denote the column vector (such as $\mathbf{c}$ and $\bar{c}$). And we denote block vector by using the bold body with head bar (such as $\bar{\mathbf{c}}$). A matrix is represented by character with double head bars (such as $\bar{\bar{c}}$).

Suppose the unknown scatterers (PEC and dielectric) are located inside the domain of interest $D \subset R^2$. The background is air and k_0 denotes the wave number in free space. A total number of N_{inc} unit plane waves that are evenly distributed around a circle impinge on the domain. The scattered field is received by N_{r} antennas, which are symmetrically located around a circle. Thus there are totally $N_{\text{r}} \times N_{\text{inc}}$ points of data recorded in the scattered field matrix. The whole domain of interest is discretized into square meshes with N subunits. If the mesh is fine enough, the scattering behavior of each cell can be well approximated by a circle of the same area such that the analytical form of *T*-matrix [25] can be used. The equivalent radius of each subunit is R and the centers are located at $\boldsymbol{\rho}_i = (r_{0,i}, \theta_{0,i})$, $i = 1, 2, \ldots, N$, under the global coordinate system.

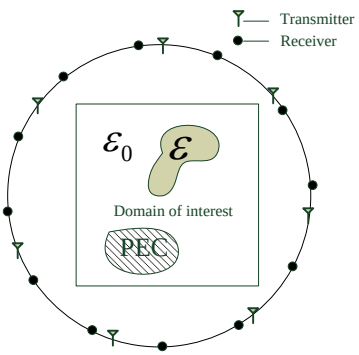

Fig.1. The geometry for inverse scattering measurements: the dielectric scatterer with permittivity ε and the PEC scatterer coexist in the domain of interest that is shown as a square.

B. Formulation of the T-matrix method

Applying the multipole expansion to both the incident field and the scattered field [25], we get the total field,

$$E_z^{\text{tot}}(\mathbf{r}) = \text{Rg}\boldsymbol{\psi}^{\text{t}}(k_0, \mathbf{r}_i) \cdot \mathbf{e}_i + \sum_{j=1}^{N} \boldsymbol{\psi}^{\text{t}}(k_0, \mathbf{r}_j) \cdot \mathbf{a}_j, \quad i = 1, 2, \ldots, N \,. \quad (1)$$

On the right hand side, the first term is the incident field and the second term indicates the scattered field from all the subunits. The observation point is at $\mathbf{r}$ with respect to the global coordinate and $\mathbf{r}_i = \mathbf{r} - \boldsymbol{\rho}_i$ is the observation point under the local coordinate of the ith sub-unit, where $\mathbf{r}_i = (r_i, \phi_i)$, $i = 1, 2, \ldots, N$. The superscript t stands for the transpose of the vector. $\left[\boldsymbol{\psi}^{\text{t}}(k_0, \mathbf{r}_i)\right]_m = H_m^{(1)}(k_0 r_i) e^{\text{i}m\phi_i}$, and Rg stands for the regular part, i.e., $\left[\text{Rg}\boldsymbol{\psi}^{\text{t}}(k_0, \mathbf{r}_i)\right]_m = J_m(k_0 r_i) e^{\text{i}m\phi_i}$, $m = -M, \ldots, M$. M is the truncation number of multipoles. Here $\mathbf{a}_j$, $j = 1, 2, \ldots, N$ are referred to as vectors of amplitude of the induced multipole. The explicit form of $\mathbf{e}_i$ is $\left[\mathbf{e}_i\right]_m = \text{i}^m e^{\text{i}k_0 r_{0,i} \cos(\theta_{0,i} - \theta_{\text{inc}})} e^{-\text{i}m\theta_{\text{inc}}}$, where θ_{inc} is the angle that the incident wave number makes with the x-axis.

The total incident field on the ith subunit can be expressed as the summation of the background incident field and the multiple scattered fields from other subunits. The translational addition theorem enables one to represent the scattered field from other scatterers as a form of the incident field to one scatterer. After some derivations by using the addition theorem [22] we get,

$$\mathbf{a}_i = \bar{\bar{T}}_i \cdot [\mathbf{e}_i + \sum_{\substack{j=1 \\ j \neq i}}^{N} \bar{\bar{\alpha}}_{ij} \cdot \mathbf{a}_j], \quad i = 1, 2, \ldots, N, \quad (2)$$

where $\bar{\bar{\alpha}}_{ij}$ is the translational matrix given in [26] and $\bar{\bar{T}}_i$ is the *T*-matrix of the ith subunit which relates the total incident field coefficient to the amplitude of the induced multipole. For a dielectric subunit, the *T*-matrix can be calculated by [25],

$$\left[T\right]_m = \frac{\sqrt{\varepsilon_{\text{r}}} J_m(k_0 R) J_m'(\sqrt{\varepsilon_{\text{r}}} k_0 R) - J_m(\sqrt{\varepsilon_{\text{r}}} k_0 R) J_m'(k_0 R)}{H_m^{(1)\prime}(k_0 R) J_m(\sqrt{\varepsilon_{\text{r}}} k_0 R) - \sqrt{\varepsilon_{\text{r}}} J_m'(\sqrt{\varepsilon_{\text{r}}} k_0 R) H_m^{(1)}(k_0 R)}, \quad (3)$$

$m = -M, \ldots, M$

And for a PEC subunit,

$$\left[T\right]_m = -\frac{J_m(k_0 R)}{H_m^{(1)}(k_0 R)}, \quad m = -M, \ldots, M \,. \quad (4)$$

Combining the N equations for all the subunits into one matrix equation, we then obtain amplitude of the induced multipole as,

$$\bar{\mathbf{a}} = \bar{\bar{O}} \cdot \left[\bar{\mathbf{e}} - \bar{\bar{A}} \cdot \bar{\mathbf{a}}\right], \quad (5)$$

where $\bar{\mathbf{a}}$ is an $N(2M+1)\times 1$ dimension vector consisting of $\mathbf{a}_i, i=1,2,\ldots,N$ along its column and $\bar{\bar{O}}$ is a square matrix of size $N(2M+1)\times N(2M+1)$, with the *T*-matrices for each subunit being arranged along its diagonal and zeros being in off-diagonal. Matrix $\bar{\bar{A}}$ is the combination of translational matrices, where $[\bar{\bar{A}}]_{ij}=-\bar{\bar{\alpha}}_{ij}$ for $i\neq j$ and zero otherwise. $\bar{\mathbf{e}}$ is an $N(2M+1)\times 1$ column vector consisting of $\mathbf{e}_i, i=1,2,\ldots,N$ along its column.

The scattered field on the receiver can be obtained by,

$$E_z^{\mathrm{sca}}(\mathbf{r}_q')=\sum_{j=1}^{N}\boldsymbol{\psi}^{\mathrm{t}}(k_0,\mathbf{r}_j')\cdot\mathbf{a}_j \tag{6}$$

where $\mathbf{r}_q', q=1,2,\ldots,N_{\mathrm{r}}$ is the location of the receiver under the global coordinate. $\mathbf{r}_j'=\mathbf{r}_q'-\boldsymbol{\rho}_j$ is the location of receiver under the local coordinate of the jth subunit.

Combining the N_{r} equations for all the receivers into one matrix equation, we have

$$\mathbf{E}^{\mathrm{sca}}=\bar{\bar{\boldsymbol{\psi}}}^{\mathrm{t}}\cdot\bar{\mathbf{a}}. \tag{7}$$

Eq.(5) and Eq.(7) are referred to as the state equation and the field equation, respectively. Note that in the EFIE model, the state and field equations are connected by the induced current, while in *T*-matrix modeling, Eqs.(5) and (7) are connected by the amplitude of induced multipole $\bar{\mathbf{a}}$.

III. Inverse Problem

Two steps are involved in the inversion scheme. The first step is to retrieve the *T*- matrices (matrix $\bar{\bar{O}}$) from the given scattering data by optimization. We use SOM as the inversion method. Attention should be paid to the multipole truncation number, which is closely related to both the accuracy and computational cost of the method. The second step is to distinguish the PEC from the dielectric scatterers and then to retrieve the relative permittivity for the dielectric scatterers, which is the key point in solving the mixed boundary problem.

A. The inversion method

The essence of original SOM lies in that it fixes one portion of the induced current first by applying singular value decomposition (SVD) to the matrix that maps the induced current to the field on receivers. Then the optimization is carried out in a smaller subspace of the current space in SOM, which results in faster convergent speed of the algorithm.

Similarly, we can also apply SOM to the *T*-matrix modeling method by first fixing one portion of the amplitude of induced multipole. The matrix $\bar{\bar{\boldsymbol{\psi}}}^{\mathrm{t}}$ of dimension $N_{\mathrm{r}}\times(2M+1)N$ in Eq.(7) refers to the mapping from amplitude of the induced multipole $\bar{\mathbf{a}}$ to the scattered field on the receivers. $\bar{\bar{\boldsymbol{\psi}}}^{\mathrm{t}}$ is defined uniquely by the domain of interest and the position of the receivers. It is a similar mapping operator as $\bar{\bar{G}}_{\mathrm{S}}$ in the EFIE model [27].

We take SVD of $\bar{\bar{\boldsymbol{\psi}}}^{\mathrm{t}}$ as $\bar{\bar{\boldsymbol{\psi}}}^{\mathrm{t}}=\bar{\bar{U}}\cdot\bar{\bar{\Sigma}}\cdot\bar{\bar{V}}^{*}$. After analyzing the spectrum of singular values, the deterministic part of $\bar{\mathbf{a}}$ can be uniquely defined by the scattered field and the first L leading singular values as $\bar{\mathbf{a}}^{\mathrm{s}}=\sum_{j=1}^{L}\frac{\bar{u}_j^{*}\cdot\bar{E}^{\mathrm{sca}}}{\sigma_j}\bar{v}_j$, where the definition of the parameters can be found in [27]. $\bar{\mathbf{a}}$ is decomposed as $\bar{\mathbf{a}}=\bar{\mathbf{a}}^{\mathrm{s}}+\bar{\mathbf{a}}^{\mathrm{n}}=\bar{\mathbf{a}}^{\mathrm{s}}+\bar{\bar{V}}^{\mathrm{n}}\cdot\bar{\alpha}^{\mathrm{n}}$, where $\bar{\bar{V}}^{\mathrm{n}}$ is composed of $(2M+1)N-L$ right singular vectors and $\bar{\alpha}^{\mathrm{n}}$ is a $(2M+1)N-L$ dimensional vector to be solved for by optimization.

Due to the truncation of the singular values, the residue of the field equation can be defined as,

$$\Delta^{\mathrm{fie}}=\left\|\bar{\bar{\boldsymbol{\psi}}}^{\mathrm{t}}\cdot\bar{\mathbf{a}}^{\mathrm{s}}+\bar{\bar{\boldsymbol{\psi}}}^{\mathrm{t}}\cdot\bar{\bar{V}}^{\mathrm{n}}\cdot\bar{\alpha}^{\mathrm{n}}-\bar{E}^{\mathrm{sca}}\right\|^2, \tag{8}$$

where $\|\cdot\|$ is the Euclidean length of a vector. Similarly, the residue of the state equation in Eq.(5) is defined to be [27],

$$\Delta^{\mathrm{sta}}=\left\|\bar{\bar{C}}\cdot\bar{\alpha}^{\mathrm{n}}-\bar{D}\right\|^2, \tag{9}$$

where $\bar{\bar{C}}=\bar{\bar{V}}^{\mathrm{n}}+\bar{\bar{O}}\cdot\bar{\bar{A}}\cdot\bar{\bar{V}}^{\mathrm{n}}$ and $\bar{D}=\bar{\bar{O}}[\bar{\mathbf{e}}-\bar{\bar{A}}\cdot\bar{\mathbf{a}}^{\mathrm{s}}]-\bar{\mathbf{a}}^{\mathrm{s}}$. The total relative residue is defined to be

$$\Delta^{\mathrm{tot}}=\Delta^{\mathrm{fie}}/\left\|\bar{E}^{\mathrm{sca}}\right\|^2+\Delta^{\mathrm{sta}}/\left\|\bar{\mathbf{a}}^{\mathrm{s}}\right\|^2. \tag{10}$$

For each incidence $\bar{E}_p^{\mathrm{inc}}$, the total relative residue can be calculated as $\Delta_p^{\mathrm{tot}}, p=1,2,\ldots,N_{\mathrm{inc}}$. The diagonal elements of matrix $\bar{\bar{O}}$ are the unknown parameters to be solved in the optimization process. It is obtained by minimizing the following cost function,

$$f(\bar{\bar{O}})=\frac{1}{2}\sum_{p=1}^{N_{\mathrm{inc}}}\Delta_p^{\mathrm{tot}}. \tag{11}$$

In solving the cost function, the two-step conjugate gradient method is applied, i.e. alternatively updating $\bar{\alpha}^{\mathrm{n}}$ and the $\bar{\bar{O}}$ matrix. The steps of the algorithm are similar to the original SOM [5] and is omitted here.

B. The choice of truncation number M

The number of unknowns in the EFIE model is the number of subunits, while the number of unknowns in *T*-matrix model is the number of subunits multiplied by number of multipoles chosen in expanding the field on each subunit. On the other hand, it is clear that the larger is the truncation number for multipoles M, the more accurate is the calculated scattered field in the *T*-matrix method. Therefore a study of the minimum value of M is critical in ensuring a balance between the accuracy of the solution and the computational cost.

Under the fine meshing assumption ($k_0R\ll 1$), the small term asymptotic approximations for elements in *T*-matrices for both dielectric and PEC subunits are shown in Table 1.

Table 1. The asymptotic approximations for elements in *T*-matrix

Dielectric	$[T]_0=\frac{\pi(k_0R)^2}{4\mathrm{i}}(1-\varepsilon_r)$	$[T]_1=\frac{\pi\mathrm{i}}{32}(\varepsilon_r-1)(k_0R)^4$
PEC	$[T]_0=\frac{\pi\mathrm{i}}{2\ln(k_0R)}$	$[T]_1=\frac{\pi}{4\mathrm{i}}(k_0R)^2$

From the approximations, we see that the monopole element is the leading term in *T*-matrices for either PEC or dielectric scatterers. $M=0$ is sufficient to represent the scattering effects on either the dielectric or the PEC subunits. However, the dipole element in *T*-matrix for PEC subunit is on the same order of k_0R as the monopole element for dielectric subunit. Therefore in the mixed boundary problem, $M=1$ should be chosen as the minimum truncation number of multipoles, to accurately represent the scattering effects on both the PEC and dielectric subunits.

To accelerate the optimization process, $M=0$ is firstly chosen to get a rough initial guess of the leading monopole elements in *T*-matrices. Then $M=1$ is used to retrieve the whole matrix $\bar{\bar{O}}$, which includes both the dipole and monopole elements. It is worth mentioning that because of the symmetric property, the two dipole elements $[T]_1$ and $[T]_{-1}$ in the *T*-matrix equal to each other. That is, the $(2i-1)$th and $(2i+1)$th elements ($i=1,2,\ldots,N$) of matrix $\bar{\bar{O}}$ should equal to each other. Thus the unknowns are reduced by one third.

C. *The classification method*

After $\bar{\bar{O}}$ is retrieved by the optimization process, the retrieved *T*-matrix for the *i*th cell can be expressed as $\bar{\bar{T}}_i$, $i=1,2,\ldots,N$, which includes the dipole elements $[T]_{\pm1}$ and the monopole element $[T]_0$. To provide the criterion for differentiating the PEC and dielectric scatterers, the monopole elements in *T*-matrices for PEC and dielectric scatterers are further studied.

The elements of *T*-matrix for dielectric scatterer is nonlinear with respect to ε_r. If the small term assumption $\left|\sqrt{\varepsilon_r}k_0R\right|<<1$ is satisfied, the monopole element for dielectric can be approximated by the linear polynomial, $[T]_0=\frac{\pi(k_0R)^2}{4\mathrm{i}}(1-\varepsilon_r)$. In this paper, we consider only dielectric scatterers with $\mathrm{real}(\varepsilon_r)>1$. Thus the imaginary part of $[T]_0$ for dielectric scatterer should be positive.

From Eq.(4), we know that the monopole element in the *T*-matrix for PEC is $[T]_0=-\frac{J_0(k_0R)}{H_0^{(1)}(k_0R)}$. Under the small term assumption $k_0R<<1$, the imaginary part of $[T]_0$ should be negative.

Therefore PEC and dielectric scatterers can be distinguished by the sign of $\mathrm{imag}([T]_0)$. The criterion is depicted as shown in Fig.2.

For those subunits identified as dielectric scatterer, the relative permittivity can be retrieved due to the fact that it is in a linear relationship with the retrieved $[T]_0$ under small term assumption,

$$[T]_0 \begin{cases} \mathrm{imag}([T]_0)>0 \longrightarrow \text{Dielectric} \\ \mathrm{imag}([T]_0)<0 \longrightarrow \text{PEC} \end{cases}$$

Fig.2. Criterion of classifying the PEC and dielectric scatterers

$$\varepsilon_r \begin{cases} \mathrm{real}(\varepsilon_r)>1 \longrightarrow \text{Dielectric} \\ \mathrm{real}(\varepsilon_r)<0 \longrightarrow \text{PEC} \end{cases}$$

Fig. 3. Criterion of classifying the PEC and dielectric scatterers in the relative permittivity pattern

$$\varepsilon_r=1-\frac{4\mathrm{i}[T]_0}{\pi(k_0R)^2}. \tag{12}$$

After further studying Fig.2 and Eq.(12), we find a convenient way to realize both differentiating PEC from dielectric scatterers and retrieving the relative permittivities for dielectric scatterers. As being indicated in Fig.2, the $[T]_0$ for PEC has a negative imaginary part. Thus from Eq.(12), the retrieved ε_r for PEC should have a real part that is less than 1. What is more, the application of L'Hôpital's rule shows that the numerical value of ε_r for PEC is much less than zero in the case when k_0R approaches 0. This means that the mathematical implementation of Eq.(12) for PEC scatterers yields a value of relative permittivity that is automatically beyond the range of relative permittivity for dielectric scatterers. In summary, the convenient way to realize both differentiating PEC from dielectric scatterers and retrieving the relative permittivities for dielectric scatterers is given out in Fig. 3. The advantage of the proposed method is that it works well no matter the dielectric scatterer is lossy or not.

IV. Numerical Results

We present five numerical examples to validate the *T*-matrix method. The first four examples are based on synthetic data. The last example is retrieved from the experimental dataset provided by Institut Fresnel (Marseille, France) [28].

The domain of interest for all the first three numerical examples under investigation is a square of size $\lambda\times\lambda$, which is discretized into $N=45\times45$ square subunits. $N_{\mathrm{inc}}=10$

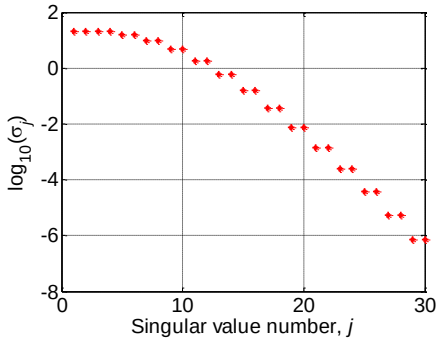

Fig. 4. Singular values of the matrix $\bar{\bar{\psi}}^t$

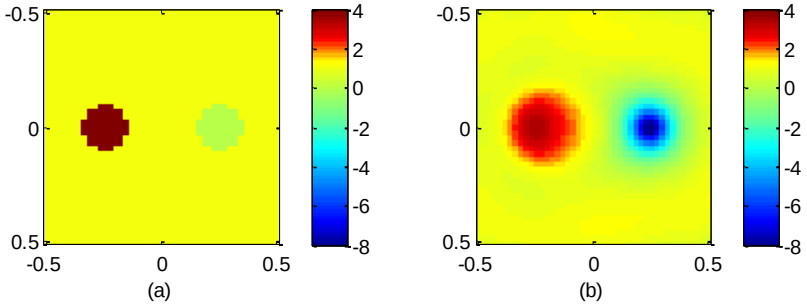

Fig. 5. Two circular objects: one PEC and one dielectric scatterer (a) original pattern. (b) Reconstructed pattern.

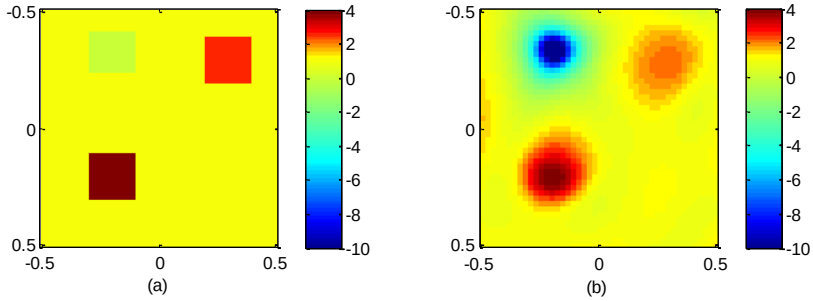

Fig. 6. Three square objects: one PEC and two dielectric scatterers with different permittivities (a) Original pattern. (b) Reconstructed pattern.

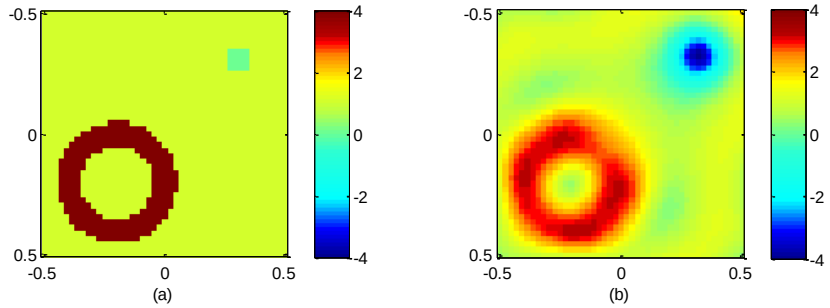

Fig. 7. A ring dielectric object and a square PEC object (a) original pattern. (b) Reconstructed pattern.

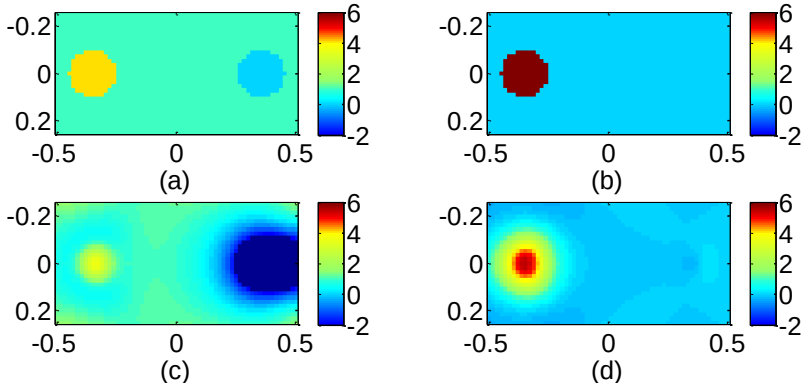

Fig. 8. Two circular objects: one PEC and one lossy dielectric scatterer. (a) Original pattern for real part of ε_r. (b) Original pattern for imaginary part of ε_r. (c) Reconstructed pattern for real part of ε_r. (d) Reconstructed pattern for imaginary part of ε_r.

plane incident waves are evenly distributed on $[0,2\pi)$. N_r=30 receivers are symmetrically located on a circle of radius 5λ. To avoid the inverse crime, the number of multipoles used in getting the forward data is more than that used in the inverse part. The synthetic data is calculated by T-matrix method with $M=2$. The scattered field is recorded in the matrix $\overline{\overline{K}}$ of size $N_r \times N_{inc}$. Then white Gaussian noise $\overline{\overline{\kappa}}$ is added to the matrix $\overline{\overline{K}}$, and the resultant noisy matrix $\overline{\overline{K}}+\overline{\overline{\kappa}}$ is treated as the measured scattered field. The noise level is quantified by the noise-to-signal ratio defined as $\frac{\|\kappa\|_F}{\|K\|_F}\times 100\%$, where $\|\cdot\|_F$ denotes the Frobenius norm of a matrix. The singular value spectrum of the matrix $\bar{\bar{\psi}}^t$ for $M=1$ is shown in Fig. 4. The value of L in cost function can be chosen according to the rules given in [4, 5].

In the inverse problem, $M=1$ is the truncation number of the multipoles. The initial guess for material in the optimization is chosen to be the air and we stop the optimization at the 100th step of iteration. In the exact permittivity patterns, we use $\varepsilon_r=0$ to mark the shape and location of PEC scatterers. Note that this practice only serves to visually distinguish PEC from other scatterers.

A. *First example*

In the first numerical example, we have two circles with radius 0.1λ placed inside the domain with center distance 0.5λ, as shown in Fig. 5(a). The PEC circular scatterer on the right side in Fig. 5 (a) is marked as $\varepsilon_r=0$ for the purpose of visualization. The dielectric circular scatterer on the left side in Fig. 5(a) has relative permittivity of $\varepsilon_r=4$. The distance of the two edges is less than half wavelength. The synthetic data includes 10% white Gaussian noise to the exact scattered field. From the reconstructed pattern shown in Fig. 5(b), the two objects are clearly identified.

B. *Second Example*

In the second example, two dielectric squares with relative permittivities $\varepsilon_r=4$ and $\varepsilon_r=2.5$ respectively are placed inside domain of interest as shown in Fig. 6 (a). A PEC square is placed on left top of the domain. 10% white Gaussian noise is added to the exact scattered field. From Fig. 6(b) we can clearly see that two dielectric objects of permittivities at around $\varepsilon_r=4$ and $\varepsilon_r=2.5$ respectively as well as a PEC object on top of the domain are well retrieved. The shape and the position of the PEC object are correctly reconstructed.

C. *Third Example*

In the third example, a dielectric ring with $\varepsilon_r=4$ is placed in the domain of interest as shown in Fig. 7(a). The outer radius is 0.25λ and inner radius is 0.15λ. A small square PEC object is placed on the upper right corner of the dielectric ring. 10% white Gaussian noise is added to the exact scattered field. From Fig. 7 (b), both the ring and PEC objects are correctly identified and the hole of the ring is clearly seen.

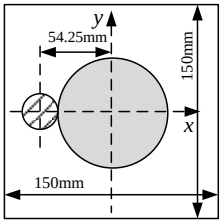

Fig. 9. Configuration of *FoamMetExt*

D. *Fourth example*

In the fourth numerical example, the domain of interest is of size $\lambda\times0.5\lambda$ and is discretized into $N=60\times30$ square subunits. The setups of the transmitters and receivers remain the same as the previous examples. We have two circles with radius 0.1λ placed inside the domain as shown in Fig. 8(a). The PEC circular scatterer is on the right side and is marked as $\varepsilon_r=0$. The dielectric circular scatterer is a lossy one with $\varepsilon_r=4+6\mathrm{i}$ and is placed on the left hand side. The original patterns for real and imaginary parts are depicted in Fig. 8 (a) and Fig. 8 (b) respectively. The synthetic data includes 10% white Gaussian noise to the exact scattered field.

From the reconstructed patterns shown in Fig. 8 (c) and Fig. 8 (d), both the lossy dielectric scatterer and PEC object are clearly identified, with the PEC on the right and dielectric on the left. The numerical example shows that the *T*-matrix method can differentiate lossy dielectric scatterer from PEC scatterer.

E. *Fifth Example*

At last, in order to verify the validity of *T*-matrix method against the experimental data, we adopt the experimental dataset collected by Institut Fresnel (Marseille, France). The

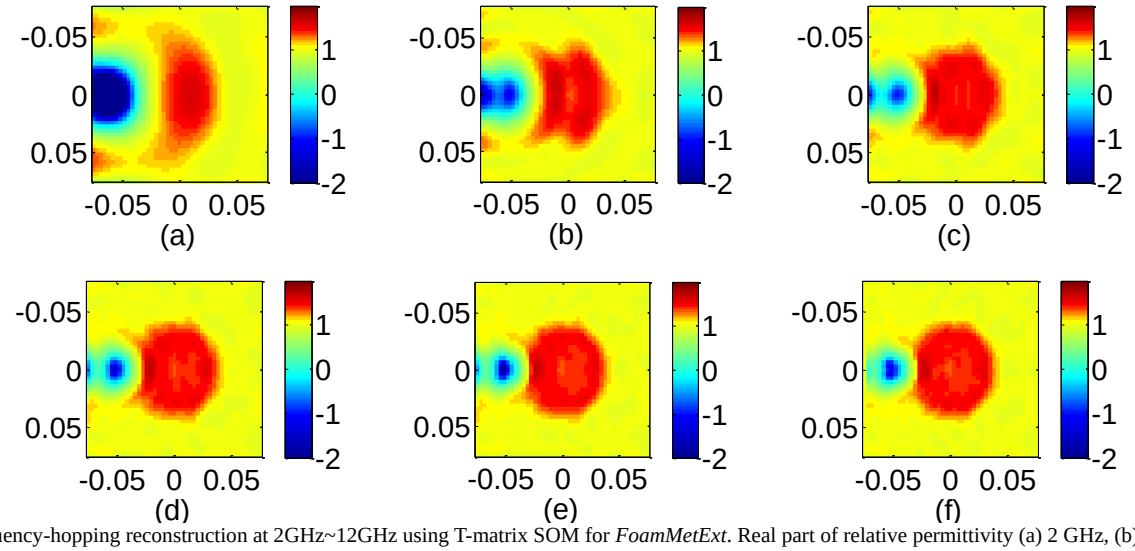

Fig. 10. Frequency-hopping reconstruction at 2GHz~12GHz using T-matrix SOM for *FoamMetExt*. Real part of relative permittivity (a) 2 GHz, (b) 4 GHz, (c) 6 GHz, (d) 8 GHz, (e) 10 GHz and (f) 12 GHz

details of the experimental configuration can be found in [28]. Here the dataset "*FoamMetExt*" is tested, where a metal is put together with foam inside the domain of interest, and we use the data that are corresponding to the two-dimensional TM illumination. The data are collected at multi-frequency illuminations.

$N_{\text{inc}} = 18$ incident waves evenly illuminate the domain around a circle of radius 1.67m. For each illumination, the scattered field is collected by 241 receiving locations no further than 60° to the transmitter with a distance of 1.67m from the origin. The configuration of the domain of interest is depicted as Fig. 9. The domain of interest is of size $150 \times 150\text{mm}^2$. A foam cylinder of diameter 80mm and $\varepsilon_{\text{r}} = 1.45 \pm 0.15$ is centered at the origin. A copper tube of diameter 28.5mm is located adjacent to the foam as shown in Fig. 9.

The inversion is done by frequency hopping within the range of 2GHz-12GHz at step of 2GHz. The domain of interest is discretized into a grid of 45x45 subunits. The unit of length in Fig. 10 is meter (m). From Fig. 10, we can see the result is quite satisfactory. The PEC and dielectric scatterers are clearly seen in Fig. 10.

V. Discussion and Conclusion

The advantage of the *T*-matrix method over the conventional quantitative method [16-19] for mixed boundary inversion is that it can well distinguish lossy dielectric scatterers from PEC because the two kinds of scatterers are distinguished by the new classification criterion rather than the imaginary part of relative permittivity.

The shortcoming of the method is the larger number of unknowns due to multipole expansion used on each subunit. When both monopole and dipole are considered, the number of unknowns is twice as many as that of conventional quantitative method. Consequently, the proposed *T*-matrix method requires higher computational cost and larger memory size. But on the other hand, the proposed method can be easily integrated with the fast multipole method that is fast and memory-saving, which will be the authors' future work.

In conclusion, this paper proposes an approach of using *T*-matrix to reconstruct the mixed boundary condition problem in two-dimensional setting. The proposed algorithm is an extension of SOM to a new modeling scheme—*T*-matrix method. Numerical results show that the proposed method works well for the mixed boundary problem. Experimental data have further proved the validity of the proposed method.

Reference:

[1] A. Abubakar, T. M. Habashy, P. M. van den Berg, and D. Gisolf, "The diagonalized contrast source approach: an inversion method beyond the Born approximation," *Inverse Problems*, vol. 21, pp. 685-702, 2005.

[2] C. Yu, L. Song, and Q. Liu, "Through-wall imaging(TWI) by radar: 2D tomographic results and analyses " *IEEE Transaction on Geoscience and Remote Sensing*, vol. 43, pp. 2793-2798, 2005.

[3] Y. Zhong and X. Chen, "Twofold subspace-based optimization method for solving inverse scattering problems," *Inverse Problems*, vol. 25, p. 085003, 2009.

[4] X. Ye and X. Chen, "The Role of Regularization Parameter of Subspace-based Optimization Method in Solving Inverse Scattering Problems," *Asia Pacific Microwave Conference, Vols 1-5*, pp. 1549-1552, 2009.

[5] X. Chen, "Subspace-based optimization method for solving inverse scattering problems," *IEEE Transactions on Geoscience and Remote Sensing*, vol. 48, pp. 42-49, 2010.

[6] X. Chen, "Subspace-based optimization method for inverse scattering problems with an inhomogeneous background medium," *Inverse Problems*, vol. 26, p. 074007, 2010.

[7] Y. Zhong, X. Chen, and K. Agarwal, "An Improved Subspace-Based Optimization Method and Its Implementation in Solving Three-Dimensional Inverse Problems," *IEEE Transactions on Geoscience and Remote Sensing*, vol. 48, pp. 3763-3768, 2010.

[8] A. Qing, C. K. Lee, and L. Jen, "Electromagnetic inverse scattering of two-dimensional perfectly conducting objects by real-coded genetic algorithm," *IEEE Transactions on Geoscience and Remote Sensing*, vol. 39, pp. 665-676, 2001.

[9] A. Qing, "Electromagnetic imaging of two-dimensional perfectly conducting cylinders with transverse electric scattered field," *IEEE Transactions on Antennas and Propagation*, vol. 50, pp. 1786-1794, 2002.

[10] A. Qing, "Electromagnetic inverse scattering of multiple two-dimensional perfectly conducting objects by the differential evolution strategy," *IEEE Transactions on Antennas and Propagation*, vol. 51, pp. 1251-1262, 2003.

[11] X. Ye, X. Chen, Y. Zhong, and K. Agarwal, "Subspace-based optimization method for reconstructing perfectly electric conductors," *Progress in Electromagnetics Research*, vol. 100, pp. 119-128, 2010.

[12] X. Ye, Y. Zhong, and X. Chen, "Reconstructing perfectly electric conductors by the subspace-based optimization method with continuous variables," *Inverse Problems*, vol. 27, p. 055011, 2011.

[13] A. F. Peterson, S. L. Ray, and R. Mittra, *Computational methods for electromagnetics*. New York: IEEE Press, 1998.

[14] D. Colton, H. Haddar, and P. Monk, "The linear sampling method for solving the electromagnetic inverse scattering problem," *SIAM Journal on Scientific Computing*, vol. 24, pp. 719-731, 2002.

[15] A. Kirsch, "The MUSIC algorithm and the factorization method in inverse scattering theory for inhomogeneous media," *Inverse Problems*, vol. 18, pp. 1025-1040, 2002.

[16] R. F. Bloemenkamp, A. Abubakar, and P. M. van den Berg, "Inversion of experimental multi-frequency data using the contrast source inversion method," *Inverse Problems*, vol. 17, pp. 1611-1622, 2001.

[17] C. Yu, L. Song, and Q. Liu, "Inversion of multi-frequency experimental data for imaging complex objects by a DTA-CSI method," *Inverse Problems*, vol. 21, pp. S165-S178, 2005.

[18] O. Feron, B. Duchene, and A. Mohammad-Djafari, "Microwave imaging of inhomogeneous objects made of a finite number of dielectric and conductive materials from experimental data," *Inverse Problems*, vol. 21, pp. S95-S115, 2005.

[19] L. Crocco, M. D'Urso, and T. Isernia, "Testing the contrast source extended Born inversion method against real data: the TM case," *Inverse Problems*, vol. 21, pp. S33-S50, 2005.

[20] P. C. Waterman, "Matrix formulation of electromagnetic scattering," *Proc. IEEE*, vol. 53, pp. 805-811, 1965.

[21] G. P. Otto and W. C. Chew, "Microwave Inverse Scattering - Local Shape Function Imaging for Improved Resolution of Strong Scatterers," *IEEE Transactions on Microwave Theory and Techniques*, vol. 42, pp. 137-141, 1994.

[22] G. P. Otto and W. C. Chew, "Inverse Scattering of H-Z Waves Using Local Shape-Function Imaging - a T-Matrix Formulation," *International Journal of Imaging Systems and Technology*, vol. 5, pp. 22-27, 1994.

[23] J. H. Lin and W. C. Chew, "Solution of the three-dimensional electromagnetic inverse problem by the local shape function and the conjugate gradient fast Fourier transform methods," *Journal of the Optical Society of America A*, vol. 14, pp. 3037-3045, 1997.

[24] K. Agarwal, L. Pan, and X. Chen, "Subspace-Based Optimization Method for Reconstruction of 2-D Complex Anisotropic Dielectric Objects," *IEEE Transactions on Microwave Theory and Techniques*, vol. 58, pp. 1065-1074, 2010.

[25] A. Z. Elsherbeni and A. A. Kishk, "Modeling of Cylindrical Objects by Circular Dielectric and Conducting Cylinders," *IEEE Transactions on Antennas and Propagation*, vol. 40, pp. 96-99,1992.

[26] W. C. Chew, *Waves and fields in inhomogeneous media*, 2nd ed. New York: IEEE Press, 1995.

[27] X. Chen, "Application of signal-subspace and optimization methods in reconstructing extended scatterers," *Journal of the Optical Society of America A*, vol. 26, pp. 1022-1026, 2009.

[28] J. M. Geffrin, P. Sabouroux, and C. Eyraud, "Free space experimental scattering database continuation: experimental set-up and measurement precision," *Inverse Problems,* vol. 21, pp. S117-S130, 2005.